

A Parameter Study of the Dust and Gas Temperature in a Field of Young Stars

Andrea Urban¹, Neal J. Evans II¹, and Steven D. Doty²

ABSTRACT

We model the thermal effect of young stars on their surrounding environment in order to understand clustered star formation. We take radiative heating of dust, dust-gas collisional heating, cosmic-ray heating, and molecular cooling into account. Using Dusty, a spherical continuum radiative transfer code, we model the dust temperature distribution around young stellar objects with various luminosities and surrounding gas and dust density distributions. We have created a grid of dust temperature models, based on our modeling with Dusty, which we can use to calculate the dust temperature in a field of stars with various parameters. We then determine the gas temperature assuming energy balance. Our models can be used to make large-scale simulations of clustered star formation more realistic.

Subject headings: Radiative Transfer; ISM: Structure; Methods: Numerical, Analytical; Stars: Formation

1. Introduction

Most of the stars in our galaxy form in groups or clusters (Lada & Lada 2003). Therefore, in order to understand the star formation history, the shape of the mass function, and the formation of massive ($M \gtrsim 5 M_{\odot}$) stars in our galaxy, the star formation process must be studied in its most common environment – a cluster. As stars form from their initial reservoir of gas and dust, they interact with their environment and heat the surrounding material, thus affecting future star formation. One of the first effects a protostar has on its environment is radiative heating from the accretion luminosity and, subsequently, nuclear

¹aurban@astro.as.utexas.edu, nje@astro.as.utexas.edu.

Department of Astronomy, University of Texas, Austin, TX 78712, USA

²doty@denison.edu.

Department of Physics and Astronomy, Denison University, Granville, OH 43023, USA

fusion. The radiation efficiently heats the dust, which in turn heats the gas through collisions. Young stars also affect their environment via strong winds and ionization, but this only occurs when they are very massive and have evolved past the very early stages of star formation. We assume that the massive stars in our sample are very young and are accreting at very high rates ($\dot{M} \gtrsim 1 \times 10^{-5} M_{\odot}/\text{yr}$). This high accretion rate allows the infalling mass to absorb all of the stellar UV photons (Churchwell 2002).

Many groups use large scale computer simulations to model clustered star formation. This is a complicated process requiring many assumptions in order to make the problem tractable. Klessen, Burkert, & Bate (1998) and Martel, Evans, & Shapiro (2006) assume that the gas is isothermal. Bate, Bonnell, & Bromm (2003) go beyond this assumption by using a barotropic equation of state. However, until recently, no one has included the effect of radiatively heating the dust and gas by the stars formed in the simulation. Krumholz, Klein, & McKee (2007) have included an approximate radiative transfer method, which works well in optically thick regions. Their method assumes that the gas temperature is equal to the dust temperature throughout their simulation. This approximation is only valid at high densities when the dust and gas are collisionally coupled. Here we develop a method that explores the effect of radiative heating and the dust and gas energetics for a range of optical depths and densities.

In our method we include various heating and cooling processes to calculate the dust and gas temperature. Stars can heat dust grains more effectively than the gas because dust grains have broad-band absorption properties. Although we will not be explicitly modeling the motion or energy density of dust grains, we assume the dust and gas are well-mixed and the dust grains transfer energy to gas particles through collisions using the energy transfer rate discussed in Young et al. (2004). The gas is heated by collisions with hot dust grains and cosmic rays. It can cool through CO and other molecular line emission.

In this paper, we calculate the dust and gas temperature in a field of stars. The dust temperature around a single source is calculated using a look-up table which we develop here. With this look-up table and an approximation to the flux-temperature conversion, we calculate the dust temperature in the field. Our look-up table is needed since the calculation of a single dust temperature distribution can take longer than a minute on current desktops and would take a substantial fraction of a large-scale simulation’s computations. Therefore we outline our method here which can be used to decrease the time spent on the calculation of the dust temperature in future studies of clustered star formation.

With the calculated value of the dust temperature, we derive the gas temperature field for a distribution of stellar sources, as in a young stellar cluster. The effect that protostars have on heating their environment using a hydrodynamic and gravity simulation will be

addressed in a future paper. In this paper, we first discuss the calculation of the dust temperature for single and multiple sources (§2), then we describe our gas temperature calculation (§3), and finally, we show some dust and gas temperature distributions when multiple sources are present (§4).

2. Dust Temperature Calculation

We consider two methods of calculating the dust temperature when there are multiple heating sources. The first approach assumes radiative equilibrium after summing up the flux of multiple sources heating a dust grain. This approach makes simplifying assumptions about the dust absorption and emission properties. The second approach uses the one-dimensional spherical radiative transfer code Dusty (Nenkova, Ivezić, & Elitzur 2000), to add up the energy density contributed by multiple sources; the dust temperature distribution is calculated separately for each source, then the temperatures are converted to energy densities (assuming radiative equilibrium), which are summed together and then converted back to a temperature. We first discuss the analytic approach (§2.1), then the numerical approach to calculating the dust temperature (§2.2), and finally we compare and analyze the two approaches (§2.3).

2.1. Analytic Dust Temperature Calculation

The rate of energy absorbed by a dust grain in a field of N stars is

$$\left(\frac{dE}{dt}\right)_{\text{abs}} = \sum_{i=1}^N \frac{R_{*i}^2}{(\Delta\mathbf{r}_{*i})^2} \int S_{\nu i} \pi a^2 Q_a(\nu) d\nu, \quad (1)$$

where R_{*i} is the radius of star i , $S_{\nu i}$ is the flux density at the stellar surface of star i (which we assume is a blackbody), Q_a is the dust grain’s absorption efficiency as a function of frequency, πa^2 is the projected surface area of the grain exposed to the star’s light, and the separation between the star i and the dust grain is

$$\Delta\mathbf{r}_{*i} = |\mathbf{r}_{*i} - \mathbf{r}|,$$

where \mathbf{r}_{*i} is the location of star i and \mathbf{r} is the position of the dust grain. Substituting in the Planck function for star i at temperature T_{*i} and assuming

$$Q_a(\nu) = Q_a(\nu_o) \left(\frac{\nu}{\nu_o}\right)^{\beta_a}, \quad (2)$$

equation (1) becomes

$$\left(\frac{dE}{dt}\right)_{\text{abs}} = \sum_{i=1}^N \frac{R_{*i}^2}{(\mathbf{r}_{*i})^2} \pi^2 a^2 \frac{Q_a(\nu_o)}{\nu_o^{\beta_a}} \frac{2h}{c^2} \left(\frac{kT_{*i}}{h}\right)^{4+\beta_a} I_{4+\beta_a}, \quad (3)$$

where

$$I_{4+\beta_a} = \Gamma(4 + \beta_a) \zeta(4 + \beta_a) \quad (4)$$

and the functions $\Gamma(x)$ and $\zeta(x)$ are defined as the gamma and Riemann zeta function.

The same assumptions can be made about the emission of the grain except that the grain emits in all directions (i.e. πa^2 becomes $4\pi a^2$), the grain is emitting instead of the star (i.e. T_{*i} becomes T_d), and the dust grain's emission efficiency is

$$Q_e(\nu) = Q_e(\nu_o) \left(\frac{\nu}{\nu_o}\right)^{\beta_e}. \quad (5)$$

These assumptions give

$$\left(\frac{dE}{dt}\right)_{\text{emis}} = \sum_{i=1}^N 4\pi^2 a^2 \frac{Q_e(\nu_o)}{\nu_o^{\beta_e}} \frac{2h}{c^2} \left(\frac{kT_d}{h}\right)^{4+\beta_e} I_{4+\beta_e}. \quad (6)$$

Assuming radiative equilibrium and removing the dependence on stellar radius with $L_* = 4\pi R_*^2 \sigma T_*^4$, T_d at position \mathbf{r} is given by

$$T_d(\mathbf{r}) = \left[\frac{1}{4} \frac{Q_a(\nu_o)}{Q_e(\nu_o)} \frac{\nu_o^{\beta_e}}{\nu_o^{\beta_a}} \frac{I_{4+\beta_a}}{I_{4+\beta_e}} \left(\frac{k}{h}\right)^{\beta_a-\beta_e} \frac{1}{4\pi\sigma} \sum_{i=1}^N \frac{L_{*i} T_{*i}^{\beta_a}}{(\Delta \mathbf{r}_{*i})^2} \right]^{1/(4+\beta_e)} \quad (7)$$

If we assume that grains absorb like graybodies ($\beta_a = 0$) where stars emit most of their luminosity (UV), then $Q_a(\nu) = Q_a(UV)$. The value of Q_e is given at $125\mu m$ with respect to Q_a . Using this approximation, we obtain

$$T_d(\mathbf{r}) = \left[3.89 \times 10^{10} \frac{Q_a(UV)}{Q_e(125\mu m)} \frac{115^{\beta_e}}{I_{4+\beta_e}} \sum_{i=1}^N \frac{L_{*i}/1L_{\odot}}{(\Delta \mathbf{r}_{*i}/1AU)^2} \right]^{1/(4+\beta_e)} \quad (8)$$

Notice that the dependence on stellar temperature disappears in this case.

The value of $Q_a(UV)/Q_e(125\mu m)$, where the UV wavelength range is $0.15\mu m - 0.30\mu m$, can be calculated from observations or from a dust grain model. We compare various values from the literature to the value derived from the dust we use in our models (see Table 1). Our dust model is a combination of OH5 dust (Ossenkopf & Henning 1994) and Pollack et al. (1994) dust as described in Young & Evans (2005). For OH5 dust, we calculate the value of

$Q_a(UV)/Q_e(125\mu m)$ assuming a 10,000K blackbody. Q_a is the stellar flux weighted average absorption efficiency of the dust and $\sigma_{\text{abs}}(\lambda)$ is the absorption cross-section for a dust grain. Therefore,

$$\frac{Q_a(UV)}{Q_e(125\mu m)} = \left(\frac{\sum_{\lambda=0.15\mu m}^{0.3\mu m} F_{\lambda} \sigma_{\text{abs}}(\lambda)}{\sum_{\lambda=0.15\mu m}^{0.3\mu m} F_{\lambda}} \right) / \sigma_{\text{abs}}(125\mu m) = 253. \quad (9)$$

Now we consider the various dust models in Table 1 and fix the value of β_e , the dust grain’s emission efficiency exponent. From equation (8), the form of the dust temperature profile becomes

$$T_d = K(\beta_e) \left[\sum_{i=1}^N \frac{L_{*i}/1L_{\odot}}{(\Delta \mathbf{r}_{*i}/1AU)^2} \right]^{1/(4+\beta_e)}, \quad (10)$$

where β_e is fixed and the values of $K(\beta_e)$ for each model are given in Table 1. In Figure 1 we compare OH5 dust to an analytic approximation (see equation 5) normalized at $125\mu m$ and vary the value of β_e . The line with $\beta_e = 1.8$ fits well at long wavelengths but not at shorter wavelengths. The opposite is true for $\beta_e = 1.0$. Since we expect long wavelength emission to dominate these clouds, we adopt an analytic approximation of OH5 dust with $\beta_e = 1.8$ as our “Analytic Solution” in the following sections.

2.2. Numerical Dust Temperature Calculation

Another method of calculating the dust temperature around multiple sources uses the code Dusty which we have set up with OH5 dust opacities (Ossenkopf & Henning 1994) using the method described in Young & Evans (2005). Dusty is a one-dimensional spherical radiative transfer code (Nenkova et al. 2000). Once a dust temperature distribution is derived around a single source, we use it to estimate the dust temperature around multiple sources, using some of the assumptions in the previous method, which we explain in more detail below. Using Dusty to calculate the dust temperature around a young star is the most accurate solution; however, this program can take over 1 minute to run for low optical depths with yet longer run times for larger τ . Therefore, we calculate the dust temperature profile for various combinations of luminosity, outer radius, and density profile to create a look-up table. (The parameters we consider are discussed in §2.2.1.) We then assume that the dust temperature profile around a single source is of the form given in equation (8), i.e.

$$T_d(\Delta \mathbf{r}_{*i}) = K_i \left(\frac{L_{*i}}{(\Delta \mathbf{r}_{*i})^2} \right)^{1/(4+\beta_i)}, \quad (11)$$

where K and β are functions of the density profile and dust properties.

This assumption is valid when the dust is optically thin. Although the gas and dust are denser closer to the central source and likely to be optically thick, we are mainly interested in the temperature distribution far from the central source where the physical processes we consider are dominant and the dust and gas are optically thin to the cloud exterior. For example, close to a forming star [$r \lesssim 1000$ AU (McCaughrean & O’dell 1996)] there may be a disk, which is not represented by our assumption of spherical symmetry. Therefore, it is not useful to model the dust temperature close to the star because it will be affected by the presence of a disk.

For each set of parameters, we run Dusty and solve for a value of K and β (see §2.2.1). Since we are only interested in the dust temperature far from the source, we fit the outer 25% of the dust temperature profile in $\log T - \log r$ space using least-squares fitting in order to determine the values of β and K in equation (11). We call these values of β and K our “Fit Solution”. In order to calculate the dust temperature of a region heated by more than one protostar, we add up the flux at the region of interest using

$$F(\mathbf{r}) = \sum_{i=1}^N \frac{L_{*i}}{4\pi(\Delta\mathbf{r}_{*i})^2} \quad (12)$$

Combining equations (11) and (12), we derive

$$F(\mathbf{r}) = \sum_{i=1}^N \frac{(T_d(\Delta\mathbf{r}_{*i})/K_i)^{4+\beta_i}}{4\pi}. \quad (13)$$

In general, we assume

$$F(\mathbf{r}) = \frac{(T_d(\mathbf{r})/\bar{K})^{4+\bar{\beta}}}{4\pi} \quad (14)$$

where \bar{K} and $\bar{\beta}$ are defined as the flux-weighted averages of the K and β values that contribute to the flux at point \mathbf{r} , i.e.

$$\bar{\beta} = \frac{\sum \beta_i L_{*i} / 4\pi \Delta\mathbf{r}_{*i}^2}{\sum L_{*i} / 4\pi \Delta\mathbf{r}_{*i}^2} \quad (15)$$

and

$$\bar{K} = \frac{\sum K_i L_{*i} / 4\pi \Delta\mathbf{r}_{*i}^2}{\sum L_{*i} / 4\pi \Delta\mathbf{r}_{*i}^2}, \quad (16)$$

where the sums are from $i = 1$ to the total number of stars, N .

Therefore, equating (13) and (14) and solving for $T_d(\mathbf{r})$ gives,

$$T_d(\mathbf{r}) = \bar{K} \left[\sum_{i=1}^N \left(\frac{T(\Delta\mathbf{r}_{*i})}{K_i} \right)^{4+\beta_i} \right]^{1/(4+\bar{\beta})}. \quad (17)$$

Using equation (11), we obtain

$$T_d(\mathbf{r}) = \bar{K} \left[\sum_{i=1}^N \frac{L_{*i}}{\Delta \mathbf{r}_{*i}^2} \right]^{1/(4+\bar{\beta})} \quad (18)$$

the equation we used to calculate the dust temperature in a field of sources.

2.2.1. Parameter Space

We assume the dust and gas are well-mixed and have the same density profile, offset only by the dust to gas mass ratio (η_{dg}) described in §3, i.e. $\rho_{\text{dust}} = \eta_{dg} \rho_{\text{gas}}$. We assume $N_{\text{H}_2}/N_{\text{He}} = 5$, which gives $\mu = 2.33$. The density profile of the gas is parameterized with n_o and α using

$$n_{\text{gas}} = n_o \left(\frac{r}{1000 \text{ AU}} \right)^{-\alpha}. \quad (19)$$

We choose an inner radius of the dust distribution to be fixed at 30AU. This number is smaller than the average sizes of more evolved disks [i.e. McCaughrean & O’dell (1996) find disk diameters of 50-1000 AU for disks in Orion], which would be considered sub-grid physics in a simulation of clustered star formation with moderate resolution. However, we find that the choice of the inner radius does not greatly affect the values of β and K for our models since we are not modeling the increase in temperature where the dust becomes optically thick.

The luminosity required to reach a dust destruction temperature of 1500 K at 30AU using the Analytic Solution is $9.58 \times 10^6 L_{\odot}$. This is outside our sample range of luminosities; therefore we can neglect the effects of dust destruction. We also vary the outer radius, r_{out} , to obtain a range of values. We find that our values of K and β do not strongly depend on r_{out} .

In all cases, the stellar input spectrum is assumed to be a blackbody with temperature $T_* = 10,000 \text{ K}$. This value does not strongly influence the output temperature distribution at outer radii since the light is quickly reprocessed by the dust to longer wavelengths.

We model the entire parameter space listed in Table 2 with two exceptions. First, we limit the density at the inner radius to be less than 10^{10} cm^{-3} , because at higher densities dynamical effects may become important since the free-fall time becomes small as the density increases. Second, we limit the mass of the envelope to be less than $\sim 1000 M_{\odot}$ since a larger envelope would likely produce a cluster of stars (assuming a star formation efficiency of 10% and a maximum stellar mass of $100 M_{\odot}$) which would break the assumption of spherical

symmetry. Therefore, combinations of large α and large n_o may not be represented in our models. Based on these restrictions, of the 5049 possible models in our parameter space, we model 3231 or 64% of them. In Figure 2 we show the luminosities and masses modeled in our parameter space. Figure 3 shows the relationship between the values of τ , α and n_o for the models in our parameter space.

2.3. Comparison of Dust Temperature Calculation Methods

Figures 4 and 5 compare the two methods of calculating the dust temperature around a single source. The Analytic Solution uses OH5 dust parameters with $\beta_e = 1.8$ as described in §2.1 which best matches the dust properties used in the Dusty Solution in Figure 1.

Figure 4 shows that the Analytic Solution captures the *shape* of the Dusty temperature profile, but at high τ it overestimates the *magnitude*. If we only vary the luminosity (see Figure 5) the offset of the Analytic Solution to the Dusty Solution changes, therefore a simple adjustment to the Analytic Solution based on luminosity would not correct the Analytic Solution. The Fit Solution described in §2.2 appears to be the best fit, as shown in Figures 4 and 5.

Figure 6 shows histograms of K and β derived from our Fit Solution for our parameter space. While most models cluster around the Analytic Solution, there is a spread that is dependent on some of the input parameters. In Figure 7 we show how the values of K and β depend on the α parameter. Models that are far from the Analytic Solution (i.e. $K = 1000$, $\beta = 0$) tend to have small values of α .

In Figures 8 and 9, we show how different parameters determine the values of K and β . Figure 8 shows that luminosity and the value of K are positively correlated. Although we have explicitly removed the luminosity dependence from equation (11), there is still some dependence of K on luminosity. This can be understood in terms of radiative trapping. For high luminosities, more photons at shorter wavelengths exist farther from the star, which increases the size of the region of high optical depth and therefore increases the value of K . Also, as α increases, K decreases. Increasing α shrinks the size of the region of high optical depth due to the buildup of material close to the star which absorbs the high energy photons. Figure 9 shows that as α decreases and luminosity increases, β moves farther from the Analytic Solution. The drastic drop of β at high luminosities can be understood by comparing the two models shown in Figure 5. In the two models, the radius at which the dust temperature turns up (i.e., when the material changes from optically thin to optically thick) moves out in radius as the luminosity increases. Since we model the value of β using only

the outer 25% of the material, we expect to be considering only the optically thin material. However, as the luminosity increases, the radius at which the transition from optically thick to optically thin material moves outward. Therefore, at higher luminosities, our calculation of β becomes influenced by the optically thick region. This is the reason β moves away from the optically thin Analytic Solution as luminosity increases.

In order to calculate values of β and K not modeled in our parameter space, we interpolate between known values in our look-up table. We use the method for interpolating in two or more dimensions described in Chapter 3 of Press et al. (1992). This method involves solving successive one-dimensional interpolations. We modified the POLIN2 subroutine to interpolate in 4 dimensions. The actual method of interpolation that we used was the polynomial interpolation method over 3 known quantities from the subroutine POLINT in Press et al. (1992). We tested our interpolation method by calculating extra models, not included in our model grid, and comparing the results between the real solution and the interpolated value. The results are tabulated in Table 3. We have varied all of the parameters by different amounts and found that the largest percent difference from the model to the interpolated value is 6.0%. The largest differences occur at the extremes of the parameter-space at small α and large luminosity. Large errors at small values of α are likely due to the large scatter of values of K and β at small α (see Figures 8 and 9). The large differences at large luminosities are probably due to the rapid change of the value of β with luminosity (see Figure 9). Although K does not change as much as β , the value of K is dependent upon the value of β .

Based on the previous discussion in this section, we use the Numerical Dust Temperature method described in §2.2 to calculate the dust temperature in the remainder of the paper. Since we are primarily interested in the dust temperature far from the luminosity source, we find that we can model the *shape* and *magnitude* of the dust temperature distribution most accurately with the Numerical Dust Temperature method. There might be some error in the calculation of K and β for models with large luminosities or small α 's. However, we don't expect very small values of α to be common (Mueller et al. 2002). Also, stars that will eventually have high luminosities are rare and will take awhile to reach this state, therefore we do not expect many stars to have high luminosities during the early stages of star formation which we model.

3. Gas Temperature Calculation

After the dust temperature as a function of distance from luminosity sources is derived for positions near stars in a cluster using the look-up table, the gas temperature can be

calculated assuming gas energetics balance. We calculate the gas temperature using a gas-dust energetics code which includes energy transfer between gas and dust via collisions, heating by cosmic rays, and molecular cooling (see Doty & Neufeld (1997) and the appendix in Young et al. (2004) for a more detailed description). We assume that the dust to gas mass ratio is $\eta_{dg} = 4.86 \times 10^{-3}$ (Hollenbach & McKee 1989) and the grain cross-section per baryon is 6.09×10^{-22} (Young et al. 2004). The cosmic ray ionization rate is $3.00 \times 10^{-17} \text{ s}^{-1}$ (van der Tak & van Dishoeck 2000) and the energy deposited per cosmic ray ionization is $2.00 \times 10^1 \text{ eV}$ (Goldsmith 2001) in our models. We take the fractional abundance of CO relative to H_2 to be 1.0×10^{-4} from Figure 8a of Lee, Bergin, & Evans (2004). We assume that the region we are studying is deep within a larger molecular cloud. Therefore, there is no interstellar radiation field impinging on the outer bounds of the cloud and the photoelectric effect on PAH's is not present.

The model dependent input parameters are T_{dust} , local density, column density, and local velocity dispersion (b). T_{dust} is calculated with the procedure described in §2.2. Local density and column density can be derived from our input density profile. The column density is calculated radially from the point of interest to the edge of the system. The edge of the system is defined as either the point at which the density is lowest or some fiducial value (as discussed later in §4). The velocity-spread parameter, b , is defined for a Maxwellian velocity distribution as $b = (2kT/m)^{1/2}$ (Spitzer 1998) and is assumed to be 1 km/s throughout this paper.

Figure 10 shows the variation of gas temperature with distance from a stellar heating source for two values of $X(\text{CO})$. Close to the source, the dust and gas temperature are coupled due to collisional interactions of the dust with the gas. As the density decreases, collisions between the dust and gas become less frequent and the gas is able to cool via molecular (mainly CO) rotational transitions. Then as the density continues to drop and there is less CO to cool the gas, cosmic ray heating becomes the dominant heating source and the gas temperature increases. For a gas with less CO ($X(\text{CO}) = 5 \times 10^{-5}$), the cooling is not as efficient and the temperature is larger. As various other parameters change in our models, different heating and cooling terms dominate and the minimum and maximum temperatures vary. We discuss this in more detail in the following section (§4).

As seen in Figure 10, the gas temperature falls below 10K when gas collisions are the dominant cooling method. Our gas cooling rate calculations are based on the work of Neufeld & Kaufman (1993) and Neufeld, Lepp, & Melnick (1995) which only extend down to 10K because the H_2 -CO collisional rates were not defined below 10K at the time of their work. We expect the cooling rate to drop drastically as the temperature approaches zero and we have attempted to adjust our cooling rate calculation to account for this. Our first

attempt to calculate the cooling rate (Λ) below 10K involved calculating the rate of change of $\log \Lambda$ with $\log T$ between 20K and 10K ($d\log\Lambda/d\log T$) and applying it to temperatures below 10K. This method has been used in Young et al. (2004) successfully when dust-gas collisions, rather than H₂-CO collisions, are the dominant mode of energy transfer at low temperatures. However, for our models, H₂-CO collisions dominate at low temperatures and to take this into account we modify the method of calculating $d\log\Lambda/d\log T$ using the Large Velocity Gradient model (LVG). Instead of extrapolating the cooling rate to low temperatures, we extrapolate the CO rate coefficients from Flower & Launay (1985) from 10K to 5K. Then we calculate $d\log\Lambda/d\log T$ between 10K and 5K using the LVG model. We apply the new values of $d\log\Lambda/d\log T$ between 10K and 5K to our gas energetics model. In Figure 10 we compare the temperature derived using the old and new method of calculating the gas temperature. Our change increases the temperature by approximately 1K at the minimum value.

4. Gas and Dust Temperature with Multiple Sources

4.1. Two Sources

In order to calculate the gas temperature between two sources, we must first calculate the dust temperature. We do this using the formalism discussed in §2.2. Once we have determined the dust temperature, we can use our energetics algorithm to calculate the gas temperature. Around each source we place a density profile. In order for this to be realistic, we choose a density, n_{eq} at which we have the two density profiles meet. The value of n_{eq} sets the distance between the sources, i.e. smaller values of n_{eq} place the sources farther apart.

Figure 11 shows the dust and gas temperature profile for increasing values of n_{eq} , i.e. smaller separations. An interesting feature of this plot is that if we only look at the region between the two sources, we find a large variation in gas temperature. This is due to the higher densities sampled as the sources move closer together. The top panel shows sources that are far apart and we see that the maximum gas temperature between the two sources is ~ 20 K and the minimum gas temperature is ~ 7 K. Cosmic ray heating, though relatively weak, can warm the material sufficiently far from luminous sources. As the sources move closer together, cosmic rays become less important until the temperature between the sources ceases to increase, whereas dust heating becomes more important and the gas is not able to cool efficiently and the minimum temperature between the sources rises.

4.2. Three Sources

Here we calculate the gas and dust temperature distribution around three sources. The three sources were placed on three of the corners of a square with sides of length 1000AU. The least luminous source was placed on the corner between the other two sources. The parameters assumed for each source are given in Table 4 as well as the position of the sources in a 2000AU x 2000AU grid. We calculate the dust temperature using the method described in §2.2 and show the results in Figure 12.

In order to determine the gas temperature, we first calculate the density (ρ) and column density (N_{col}) at each point in the grid due to all three sources, individually. Then, at each point we choose the source which gives the highest value of N_{col} and use that source to calculate N_{col} , ρ , and the gas temperature.

In order to calculate N_{col} , we integrate from the point of interest to the “edge” in the direction radially away from the source. We tested two methods of defining the “edge.” Our first method, the “Length of Square Method,” integrates from the point of interest to 2000AU from the source (Figure 13 and 14). The value of 2000 AU was chosen to equal the length of the side of the square in which we place our sources. Our second method, the “Edge of Square Method,” integrates from the point of interest to the edge of the region studied (Figure 15 and 16). Using this method, the integration length depends on the direction of integration. In both cases, we find that the gas and dust temperature are not equal, unless we are in a region of high density close to a luminosity source as seen in Figures 13 and 15. In these high density regions, the dust and gas temperature are coupled through collisions. As the density decreases, the gas temperature drops rapidly, compared to the dust temperature, due to the ability of the gas to cool through molecular transitions. Another interesting feature of these plots is the detectability of Source 1, the dimmest object in the region, even though it is close to Source 2, the brightest source in the region.

Two differences between the two methods of calculating N_{col} are evident in Figures 12 - 15. The first is the the square shape of the contours near the edges when using the Edge of Square Method in Figure 15. This is an artifact of a square region of interest. The second difference is the gas temperature near Source 1. It appears to be shifted in the direction of Source 2 for the Length of Square Method (Figure 13) and is shifted in the opposite direction for the Edge of Square Method (Figure 15). For both methods, the dust temperature and gas-dust collisional heating is the same in this region. Therefore, the molecular cooling rate and the column density must be different. For the Length of Square Method the calculation of N_{col} is dominated by Source 2 near Source 1. This is the reason the gas temperature contour around Source 1 is shifted toward Source 2. The value of N_{col} drops as we move across Source 1. This causes a shift in the gas temperature toward Source 2 even though the

dust temperature on either side of Source 1 is symmetric. For the Edge of Square Method, Source 1 is able to increase the value of N_{col} on the side facing away from Source 2 over the value calculated from Source 2. This increase in N_{col} causes the gas temperature to increase as well. Although neither of these methods is entirely correct, we use the Length of Square Method (adjusted for the size of the square) in the following figures due to the square edge effects of the Edge of Square Method.

In Figure 17, we compare the gas and dust temperature far from the sources when we replace the three sources with a single source at the location of Source 2. We use the same parameters as Source 2 for our single source, however we have increased its luminosity to $130L_{\odot}$. This figure illustrates the difficulty in determining the number of sources responsible for heating the gas and dust and highlights the need for adequate spatial resolution.

In Figure 18, we have zoomed out of the region of interest. Notice that the dust temperature steadily decreases as the distance from the central three sources increases. Yet, the gas temperature slowly begins to rise. This is due to the decrease of effectiveness of CO cooling and the increase in heating by cosmic rays as the density decreases.

5. Conclusion

We have presented a method for calculating the dust and gas temperature between stellar sources. The analytic method that we investigated for calculating the dust temperature was not accurate enough. Instead, our chosen method of calculating the dust temperature uses a simple radiative transfer code which we use to create a look-up table. Once we have derived the dust temperature, we are able to calculate the gas temperature by balancing various energy processes. We include dust-gas collisional heating, molecular cooling, and cosmic-ray heating. When we have balanced the energies, we are able to derive the gas temperature. Other methods which set the gas temperature and dust temperature equal assume the gas and dust are opaque everywhere, which is not always true. In Figure 19, we show the percentage difference between the gas and dust temperature, as well as the density, for the distribution of sources discussed in §4.2. These two figures show that the largest percentage difference between the dust and gas temperature occurs where the density is the lowest. Therefore, at low densities ($n \lesssim 10^5 \text{cm}^{-3}$), assuming equal dust and gas temperatures is not appropriate.

We plan to use the method discussed in this paper to model a region of clustered star formation with the three-dimensional hydrodynamics code discussed in Martel et al. (2006). Our method of calculating the gas and dust temperature distribution in a field of young stars

will enable us and others to more accurately model clustered star formation observationally and in future simulations.

6. Acknowledgments

AU would like to thank the NASA GSRP for providing support and Chad Young and Jeong-Eun Lee for help with DUSTY and the gas energetics code. NE would like to thank the NSF for grants AST-0307250 and AST-0607793. This work was partially supported by a grant from The Research Corporation (SDD).

REFERENCES

- Bate, M. R., Bonnell, I. A., & Bromm, V. 2003, *MNRAS*, 339, 577
- Churchwell, E. 2002, *ARA&A*, 40, 27
- Doty, S. D., & Neufeld, D. A. 1997, *ApJ*, 489, 122
- Flower, D. R., & Launay, J. M. 1985, *MNRAS*, 214, 271
- Goldsmith, P. F. 2001, *ApJ*, 557, 736
- Hildebrand, R. H. 1983, *QJRAS*, 24, 267
- Hollenbach, D., & McKee, C. F. 1989, *ApJ*, 342, 306
- Klessen, R. S., Burkert, A., & Bate, M. R. 1998, *ApJ*, 501, L205
- Krumholz, M. R., Klein, R. I., & McKee, C. F. 2007, *ApJ*, 656, 959
- Lada, C. J., & Lada, E. A. 2003, *ARA&A*, 41, 57
- Lee, J.-E., Bergin, E. A., & Evans, N. J., II 2004, *ApJ*, 617, 360
- Makinen, P., Harvey, P. M., Wilking, B. A., & Evans, N. J., II. 1985, *ApJ*, 299, 341
- Martel, H., Evans, N. J., II, & Shapiro, P. R. 2006, *ApJS*, 163, 122
- McCaughrean, M. J., & O’dell, C. R. 1996, *AJ*, 111, 1977
- Mueller, K. E., Shirley, Y. L., Evans, N. J., II, & Jacobson, H. R. 2002, *ApJS*, 143, 469
- Nenkova, M., Ivezić, Ž., & Elitzur, M. 2000, *ASP Conf. Ser.* 196: Thermal Emission Spectroscopy and Analysis of Dust, Disks, and Regoliths, 196, 77
- Neufeld, D. A., & Kaufman, M. J. 1993, *ApJ*, 418, 263
- Neufeld, D. A., Lepp, S., & Melnick, G. J. 1995, *ApJS*, 100, 132
- Ossenkopf, V., & Henning, T. 1994, *A&A*, 291, 943
- Press, W. H., Teukolsky, S. A., Vetterling, W. T., & Flannery, B. P. 1992, Cambridge: University Press, —c1992, 2nd ed.,
- Pollack, J. B., Hollenbach, D., Beckwith, S., Simonelli, D. P., Roush, T., & Fong, W. 1994, *ApJ*, 421, 615

- Spitzer, L. 1998, *Physical Processes in the Interstellar Medium*, by Lyman Spitzer, Wiley-VCH, May 1998.
- van der Tak, F. F. S., & van Dishoeck, E. F. 2000, *A&A*, 358, L79
- Young, C. H., & Evans, N. J. 2005, *ApJ*, 627, 293
- Young, K. E., Lee, J.-E., Evans, N. J., Goldsmith, P. F., & Doty, S. D. 2004, *ApJ*, 614, 252

Table 1. Dust Parameters

Dust Type	$\frac{Q_a(UV)}{Q_c(125\mu m)}$	$K(1)$	$K(1.8)$	$K(2)$
OH5 (our dust model)	253	539.3	351.1	319.8
Hildebrand (1983)	4000	936.6	565.1	506.6
Makinen et al. (1985)	790	677.1	427.2	386.7

Table 2. Dust Model Parameters

Parameter	Lower Limit	Upper Limit	Δ^a	N ^b
$\log (L/L_\odot)$	-2	6	0.5	17
$\log (n_o/1\text{cm}^{-3})$	2.5	7.5	0.5	11
α	0	4	0.5	9
$\log (r_{out}/1 \text{ pc})$	-1	0	0.5	3

^aSpacing of parameters

^bNumber of parameters

Table 3. Dust Model Interpolation Results

$L(L_\odot)$	$n_o \text{ (cm}^{-3}\text{)}$	α	$r_{out} \text{ (pc)}$	K^{model}	$K^{poly-interp}$	$K^{\%-diff}$	β^{model}	$\beta^{poly-interp}$	$\beta^{\%-diff}$
1.8×10^{-2}	5.62×10^2	1.75	0.177	302.1	300.8	0.4	1.82	1.82	0.0
1.0×10^0	5.00×10^3	2.75	0.194	214.8	213.9	0.4	1.81	1.81	0.0
1.0×10^0	5.00×10^3	1.75	0.194	295.6	295.1	0.2	1.78	1.78	0.0
1.0×10^0	5.00×10^2	0.80	0.194	322.4	310.0	3.8	1.68	1.78	6.0
1.0×10^0	5.50×10^5	2.00	0.194	161.5	157.6	2.4	1.82	1.81	0.5
1.5×10^5	5.00×10^2	2.00	0.194	355.8	356.5	0.2	1.37	1.36	0.7

Table 4. Source Parameters

Source	Luminosity (L_\odot)	$n_o(\text{cm}^{-3})$	α	$r_{out} \text{ (pc)}$	K	β	x (AU)	y (AU)
1	1	10^3	2	0.1	302.60	1.7875	500	1500
2	100	10^5	2	0.1	215.89	1.7623	1500	1500
3	10	10^4	2	0.1	263.22	1.7817	500	500

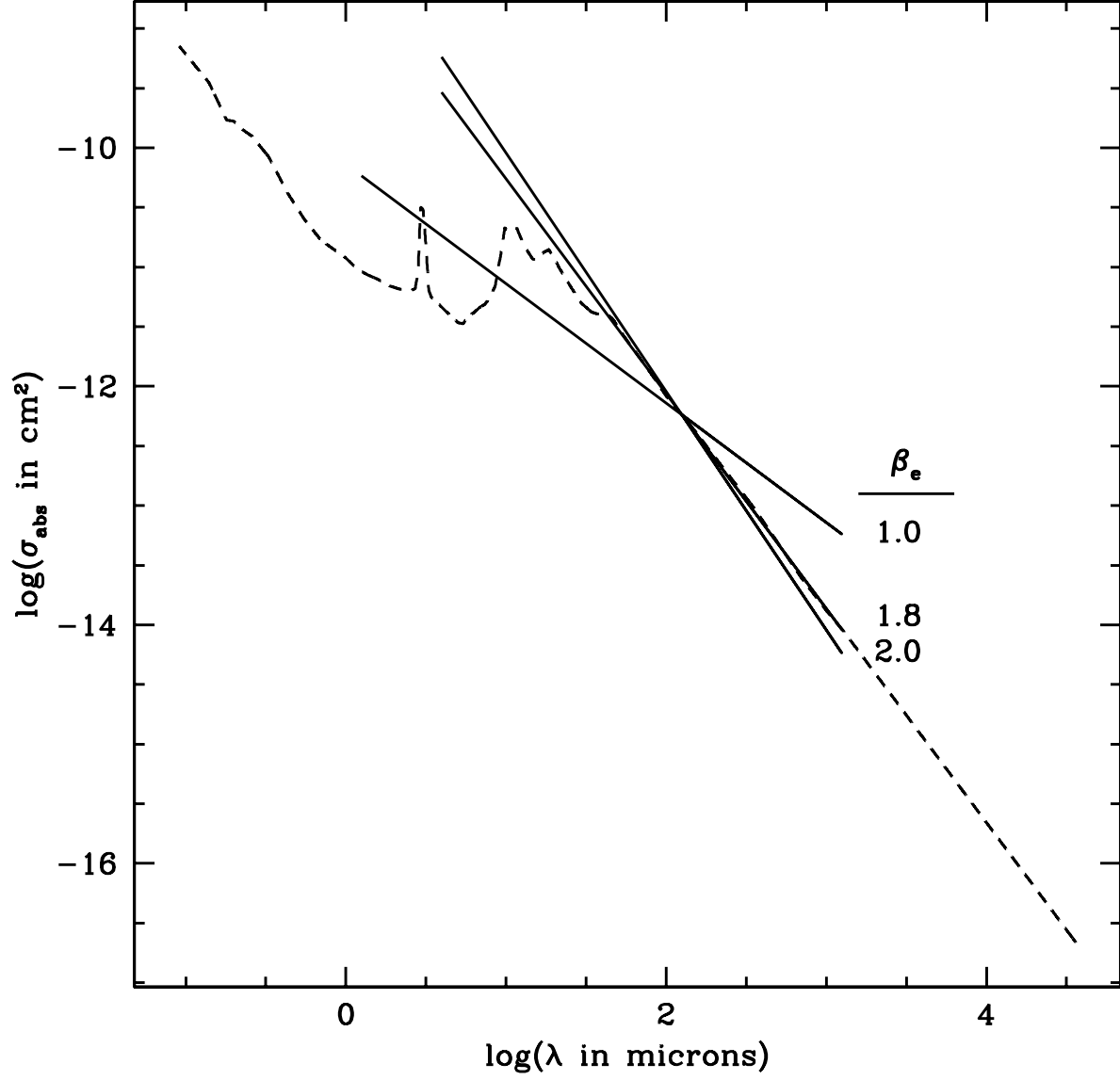


Fig. 1.— OH5 dust properties. Dashed line shows the variation of cross-section with wavelength for OH5 dust. The solid lines show the different values of β_e normalized at $125 \mu\text{m}$ that we consider in Table 1.

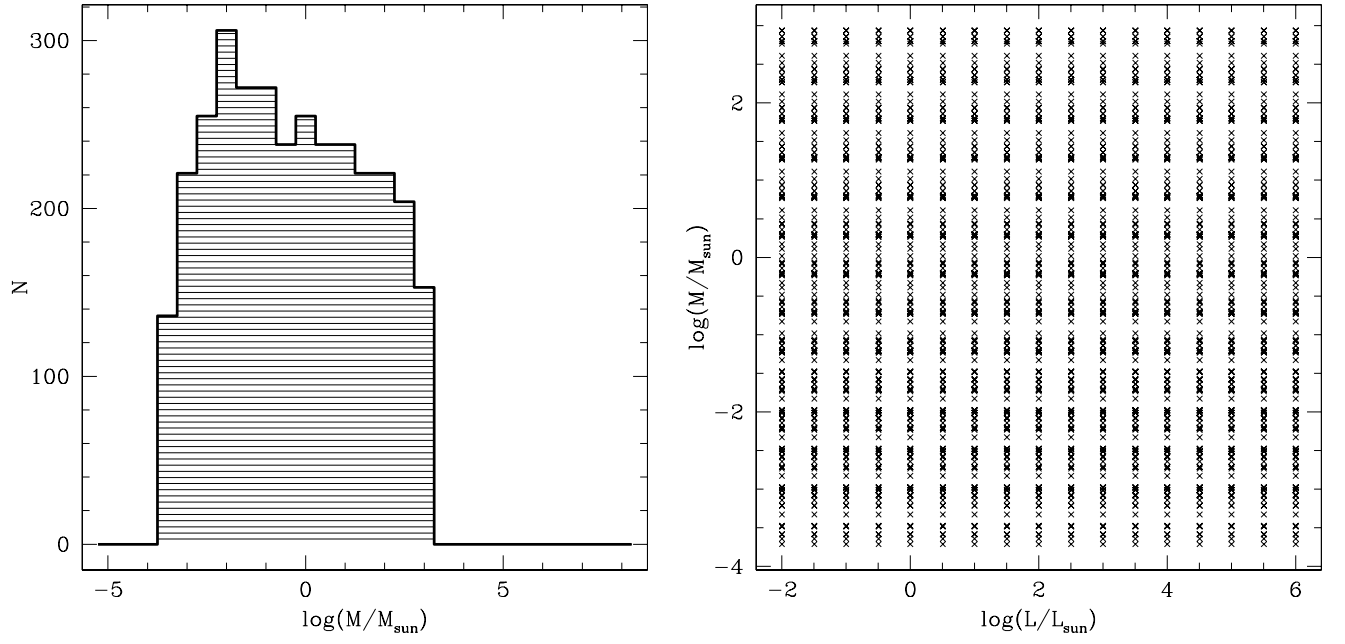


Fig. 2.— Masses and luminosities of models in our parameter space. Figure on the left shows a histogram of the masses of the clouds surrounding a source. On the right, the relationship between the mass and luminosity of all our models is plotted. For every density distribution in our sample, we have models which correspond to all of the luminosity values in our parameter space.

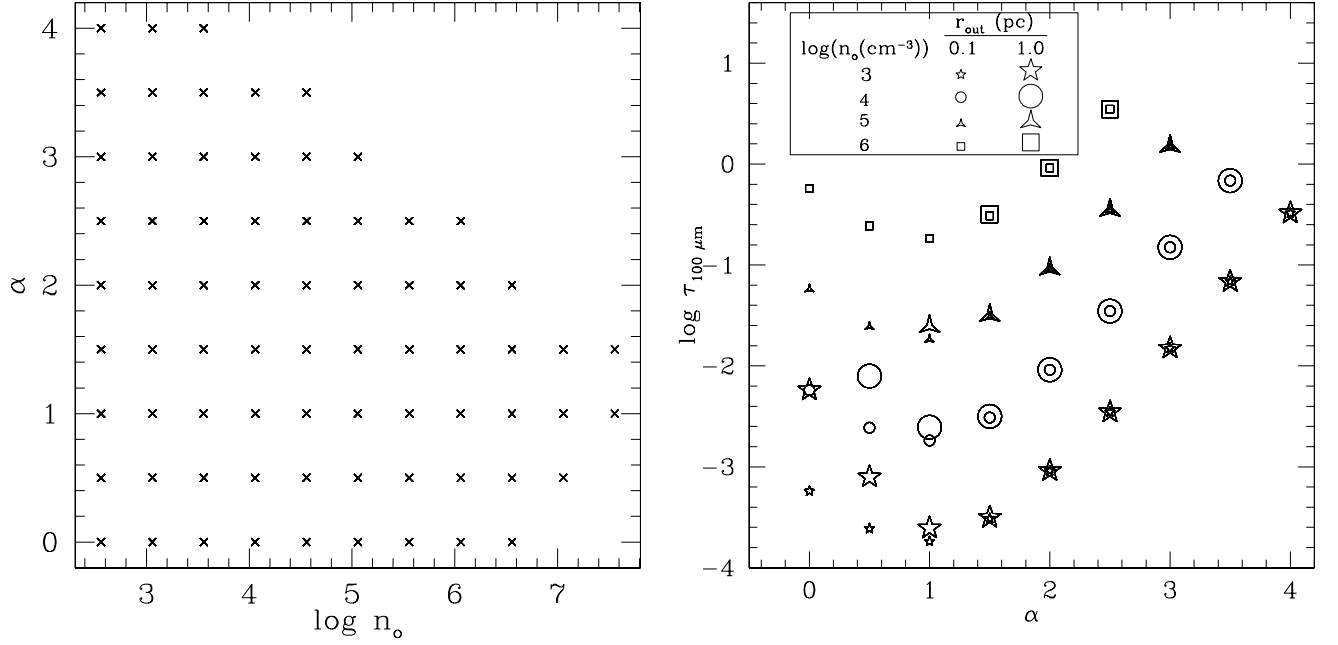


Fig. 3.— Relationship between α , τ , and n_o . The figure on the left shows the relationship between α and n_o for all our models. Some models at low α with high values of n_o are not in our sample due to the maximum mass criterion. Models missing in the top right corner of the figure at high n_o and high α are missing due to the criterion which sets the maximum density at the inner radius. On the right, we show how τ varies with α , n_o , and r_{out} for our models. At a fixed value of n_o , as α increases (and $\alpha > 1$), τ increases as well due to the sharp density increase in the profile. For lower values of α ($\alpha < 1$), τ begins to increase again, but this increase depends on amount of material included in the profile at the edge, i.e. the value of r_{out} .

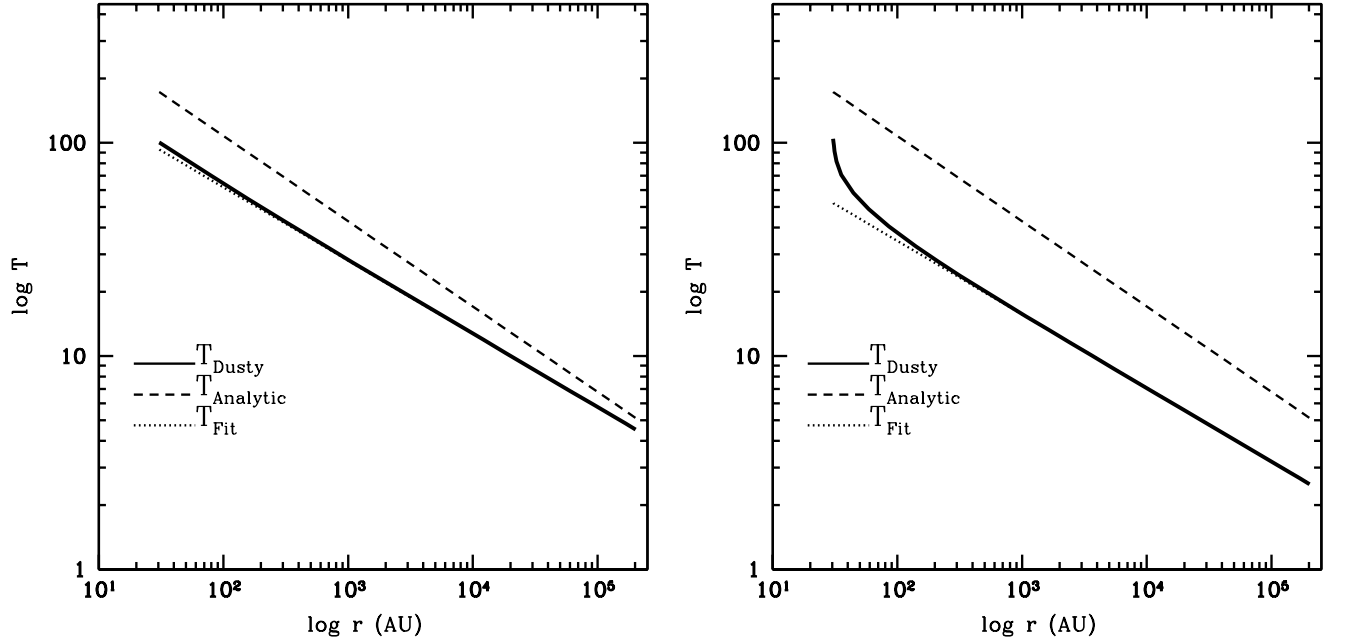


Fig. 4.— Comparison between temperature distributions for two different models with a low and high fiducial density. For both models, $L = 1L_{\odot}$, $\alpha = 2$, and $r_{\text{out}} = 1$ pc. The figure on the left has $\log n_o = 2.5$ and $\tau = 2.894 \times 10^{-4}$. The fit parameters are $K = 300.79$ and $\beta = 1.822$. The figure on the right has $\log n_o = 5.5$ and $\tau = 2.894 \times 10^{-1}$ with $K = 169.5$ and $\beta = 1.799$. Although both of these models are optically thin, as assumed in the Analytic Solution, it is clear that it is not a good description of the dust temperature. If we were to change the value of K assumed in the Analytic Solution, we might be able to fit the exact solution provided by Dusty for one model, but it would then not fit for another model.

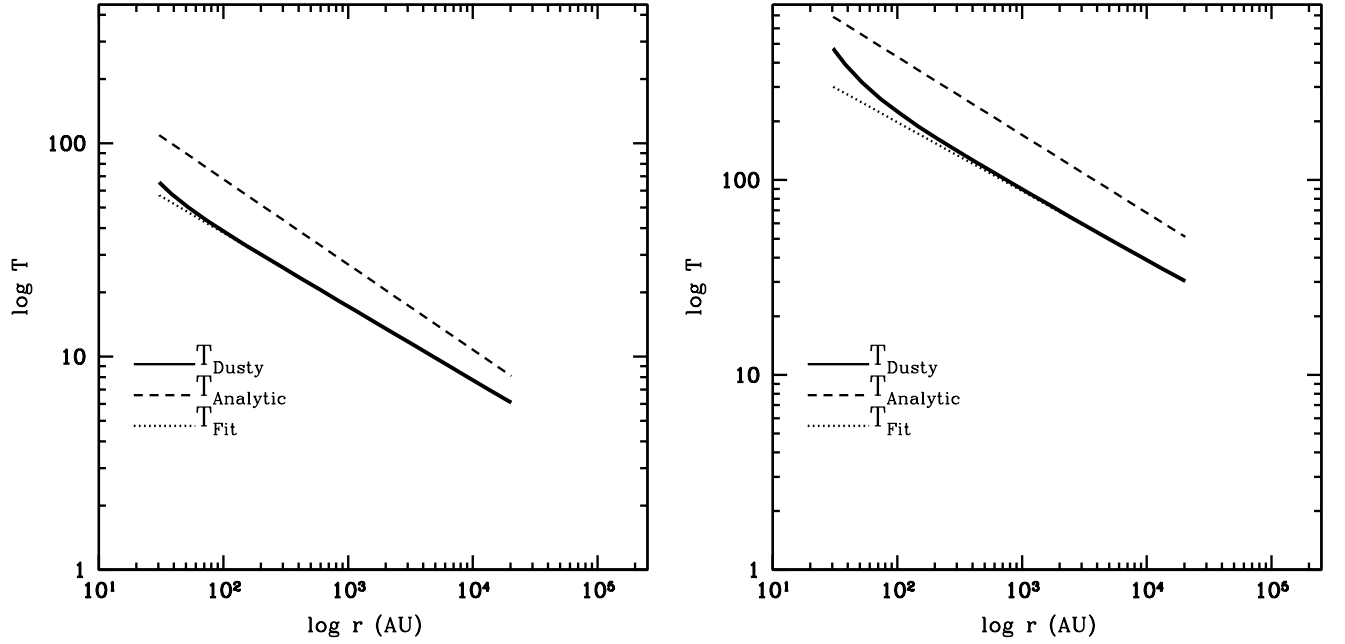


Fig. 5.— Comparison between temperature distributions for two different models with a low and high luminosity. For both models, $\alpha = 3$, and $r_{out} = 0.1$ pc, $\log n_o = 2.5$. The figure on the left has $\log L/L_\odot = -1$. The fit parameters are $K = 276.23$ and $\beta = 1.802$. The figure on the right has $\log L/L_\odot = 3$ with $K = 297.5$ and $\beta = 1.658$. These models show how increasing the luminosity increases the overall dust temperature as well as making the optically thick region near the center extend farther out.

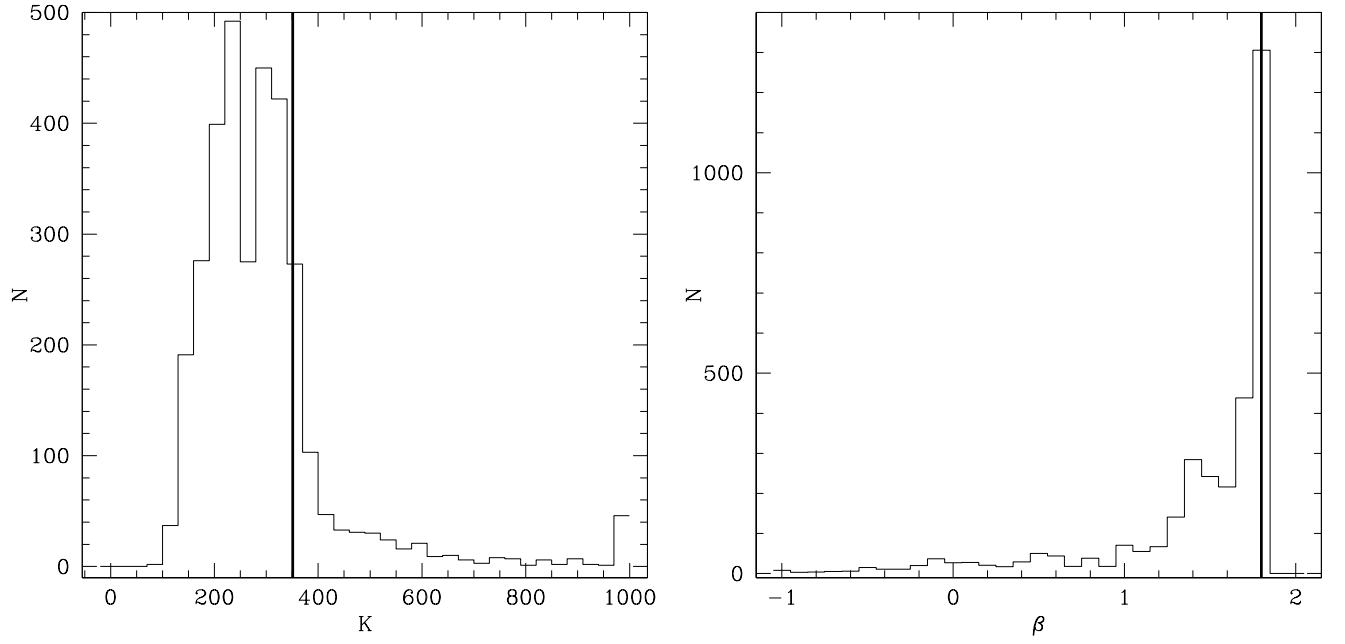


Fig. 6.— Figures shows the range of K and β for the chosen parameters in Table 2. The vertical line marks the values of K and β_e in the Analytic Solution.

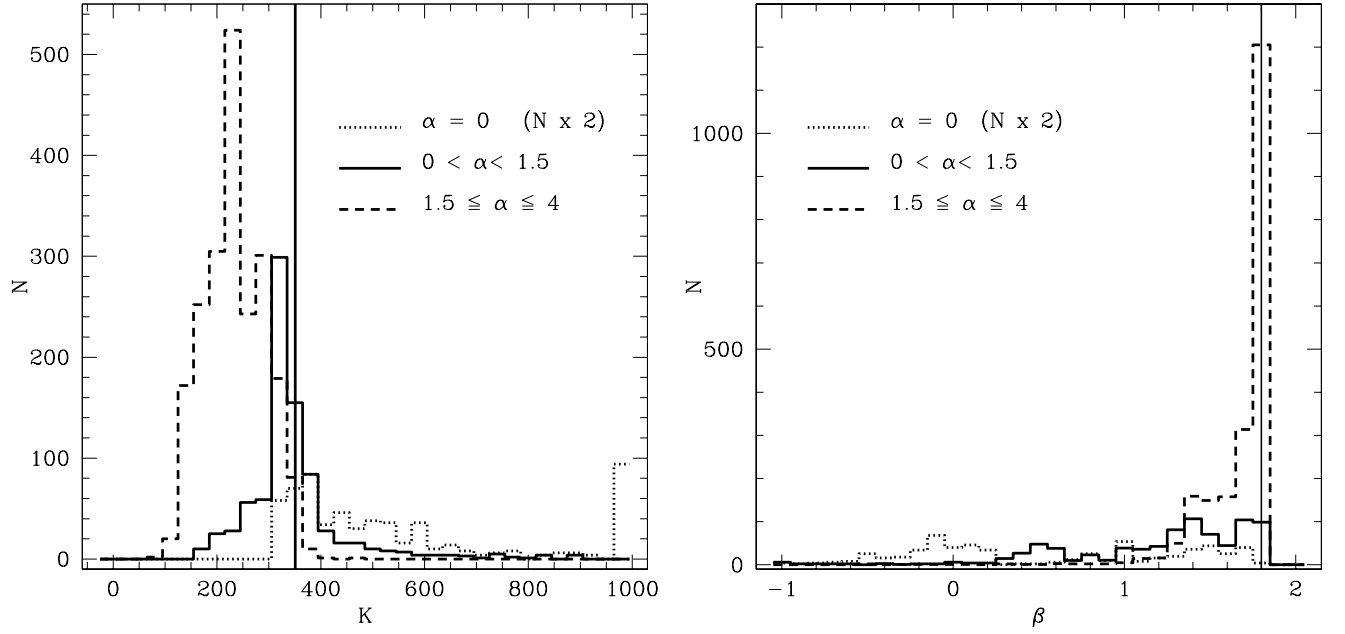


Fig. 7.— The range of K and β for the chosen parameters in Table 2 as a function of α . The vertical line marks the values of K and β_e in the Analytic Solution. Histograms for $\alpha = 0$ have been multiplied by 2 for clarity.

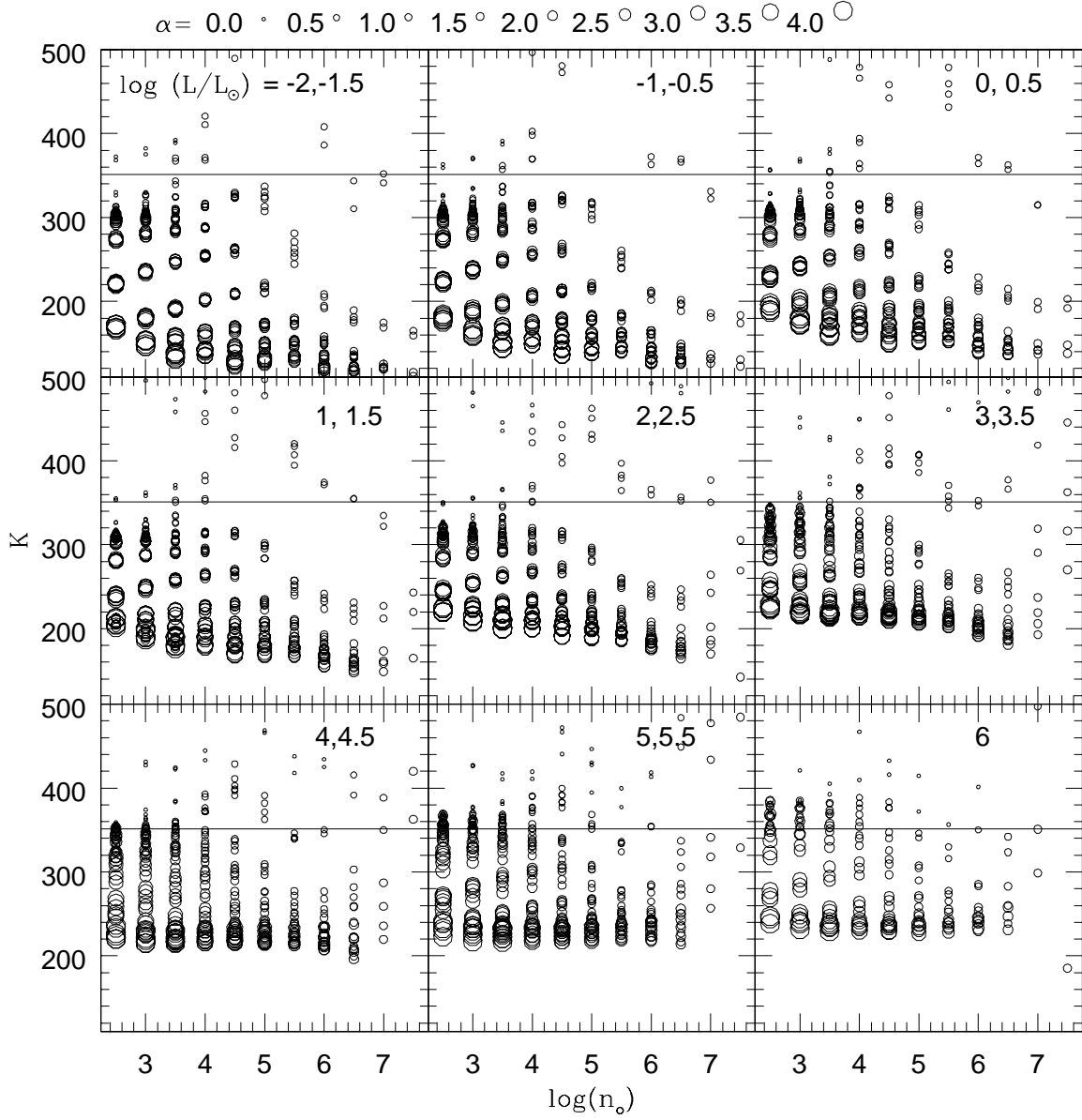


Fig. 8.— The horizontal line marks the value of K in the Analytic Solution. Individual models are plotted as circles of various sizes. The size of the circle indicates the value of the α parameter as noted in the top of the plot. The nine separate plots each show K as a function of n_o for nine different luminosity regimes. In the top-left box, $\log L/L_\odot$ is -2 or -1.5 , as indicated at the top-right corner in the box. The bottom-right box shows models with the highest luminosities.

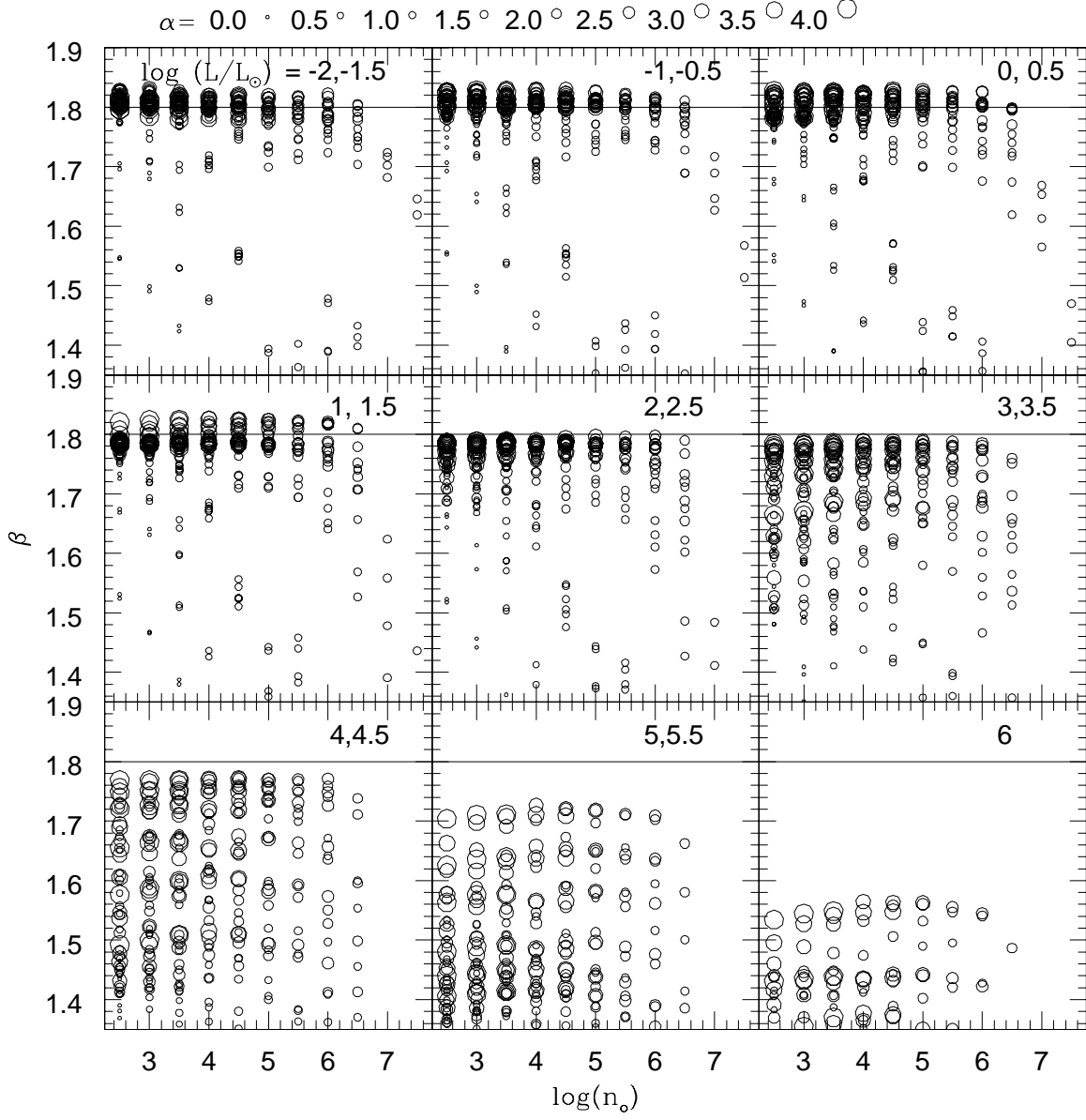


Fig. 9.— The horizontal line marks the value of β_e in the Analytic Solution. Same plot details as Figure 8 except β is plotted rather than K .

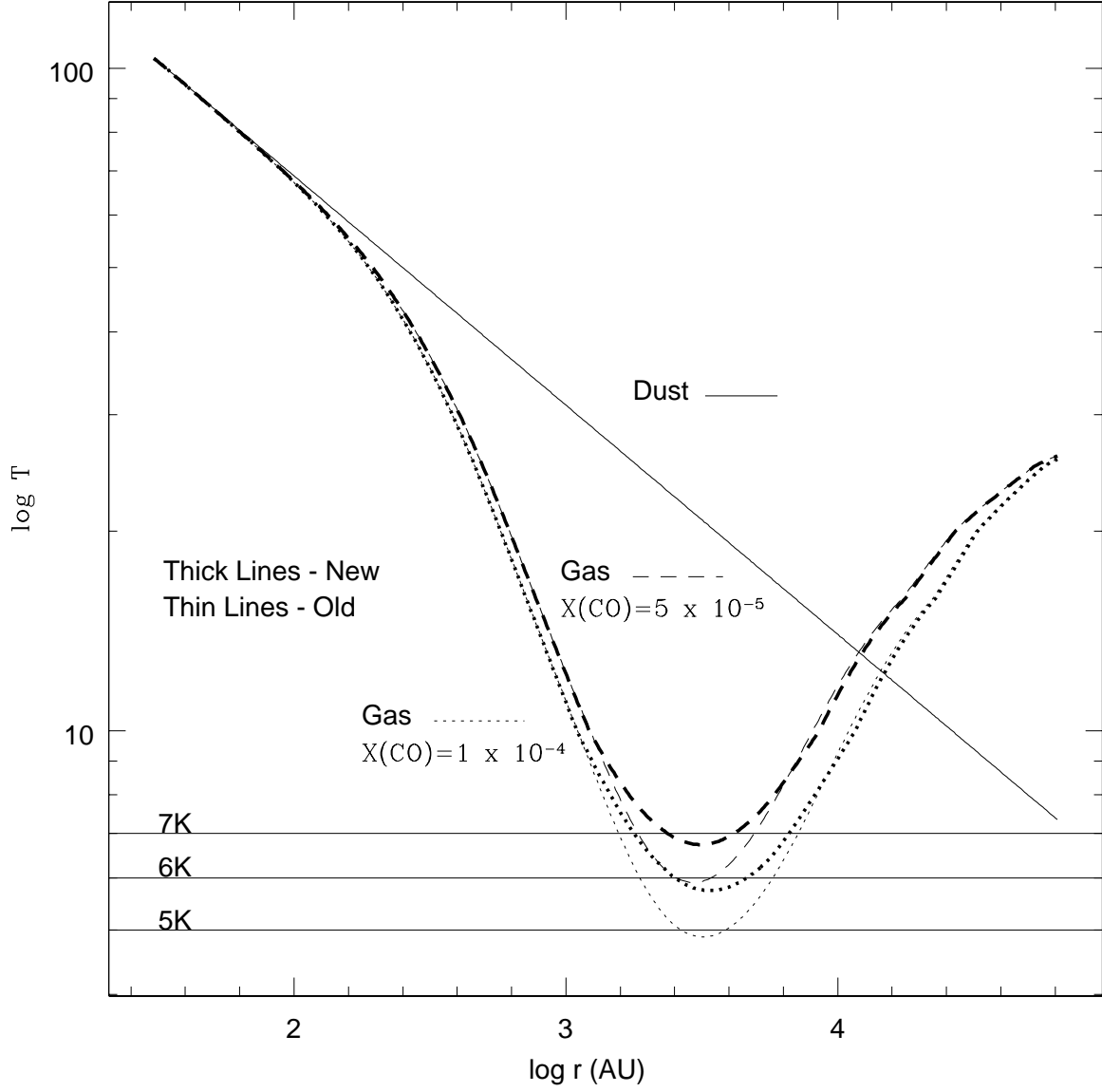


Fig. 10.— Gas temperature distribution and comparison of old and new cooling rates. Solid line shows Fit Solution to dust temperature. The model parameters are $\log (L/L_{\odot} = 1)$, $\log (r_{out}/1pc) = -0.5$, $\log n_o = 4.5$, and $\alpha = 2.5$. Dashed and dotted line show gas temperature for $X(\text{CO})=1 \times 10^{-4}$ and $X(\text{CO})=5 \times 10^{-5}$, respectively. Old and new cooling rates are shown in the thin and thick lines, respectively.

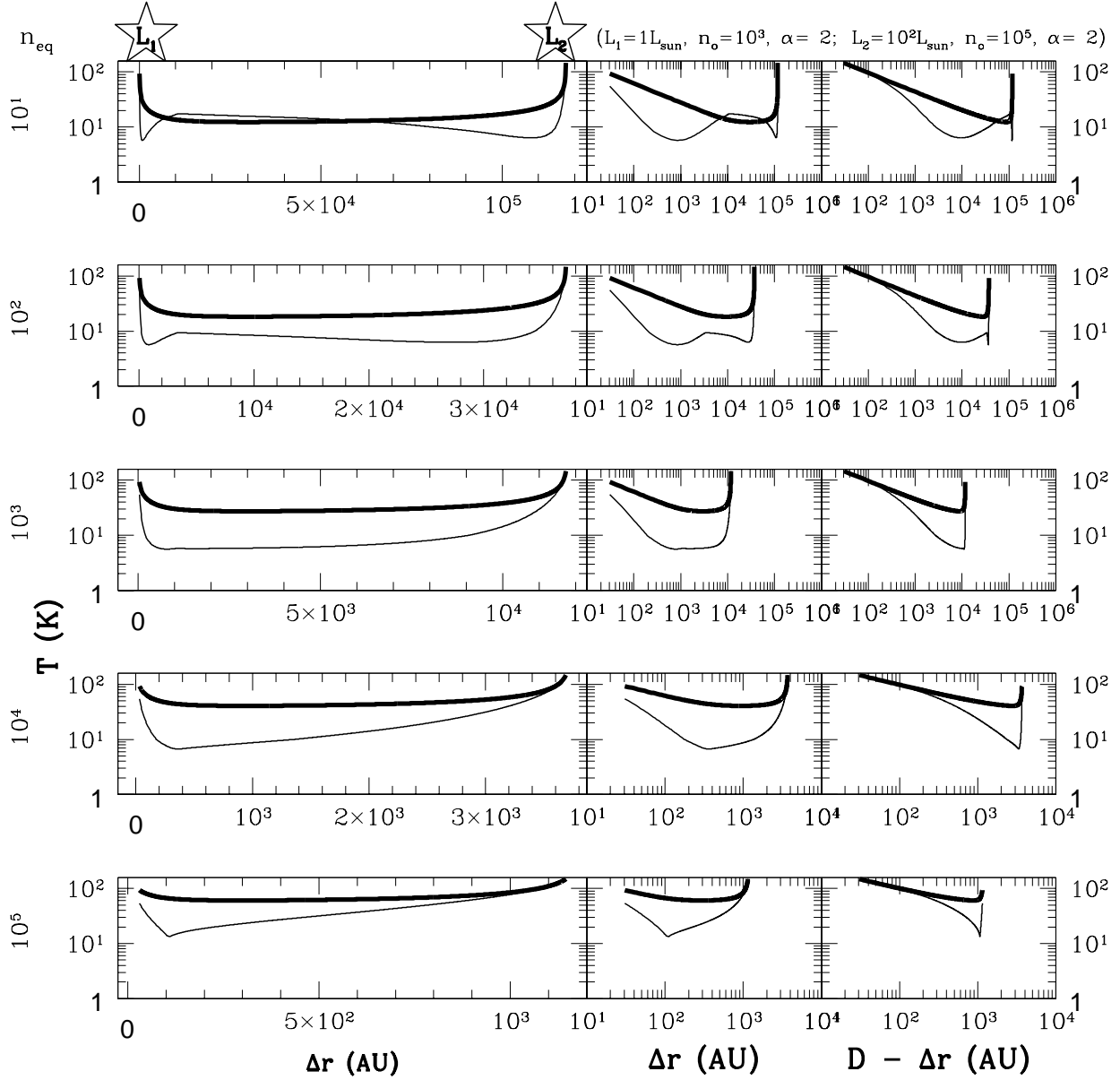


Fig. 11.— Gas temperature distribution between two sources. Plots show dust (thick line) and gas (thin line) temperature as a function of distance between two stellar sources. From top to bottom, distance between sources is decreasing, such that the gas density surrounding the two sources agrees with the value, n_{eq} quoted on the left. The source on the left (1) has the parameters $L = 1L_{\odot}$, $n_o = 10^3$, and $\alpha = 2$. The right source (2) has $L = 10^2L_{\odot}$, $n_o = 10^5$, and $\alpha = 2$. The three horizontal plots for the different values of n_{eq} show the same data from different perspectives. The large plot on the left is plotted on a linear scale from Source 1. The two smaller plots on the right are plotted on a logarithmic scale, from the perspective of Source 1 (middle) and Source 2 (right). This is done to show structure close to the individual sources.

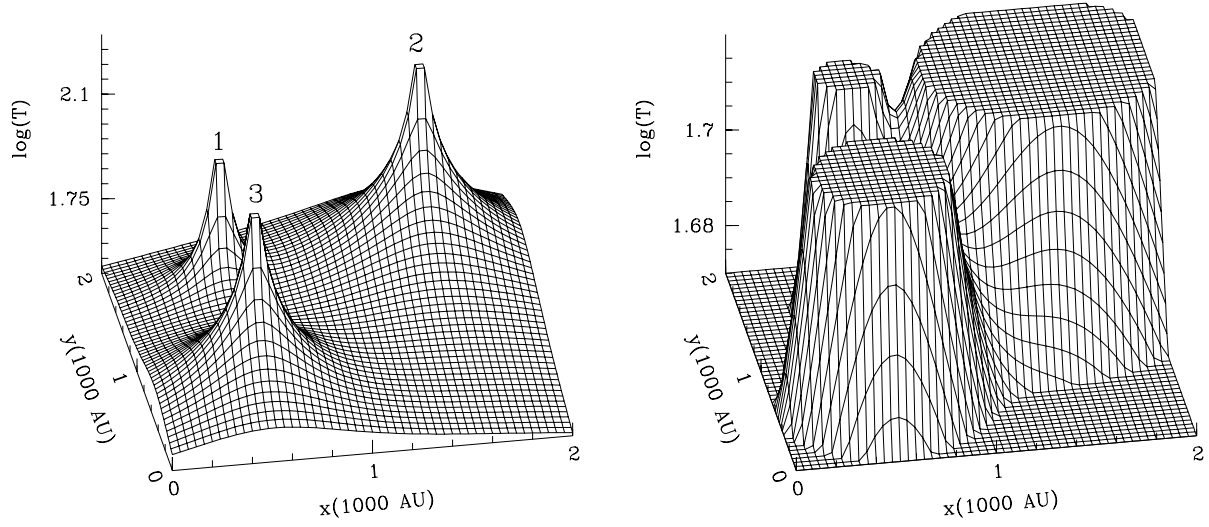


Fig. 12.— Surface plots of dust temperature. Sources are labeled according to the parameters listed in Table 4. The first figure shows the full range of dust temperatures and the second figure shows a smaller range of dust temperatures.

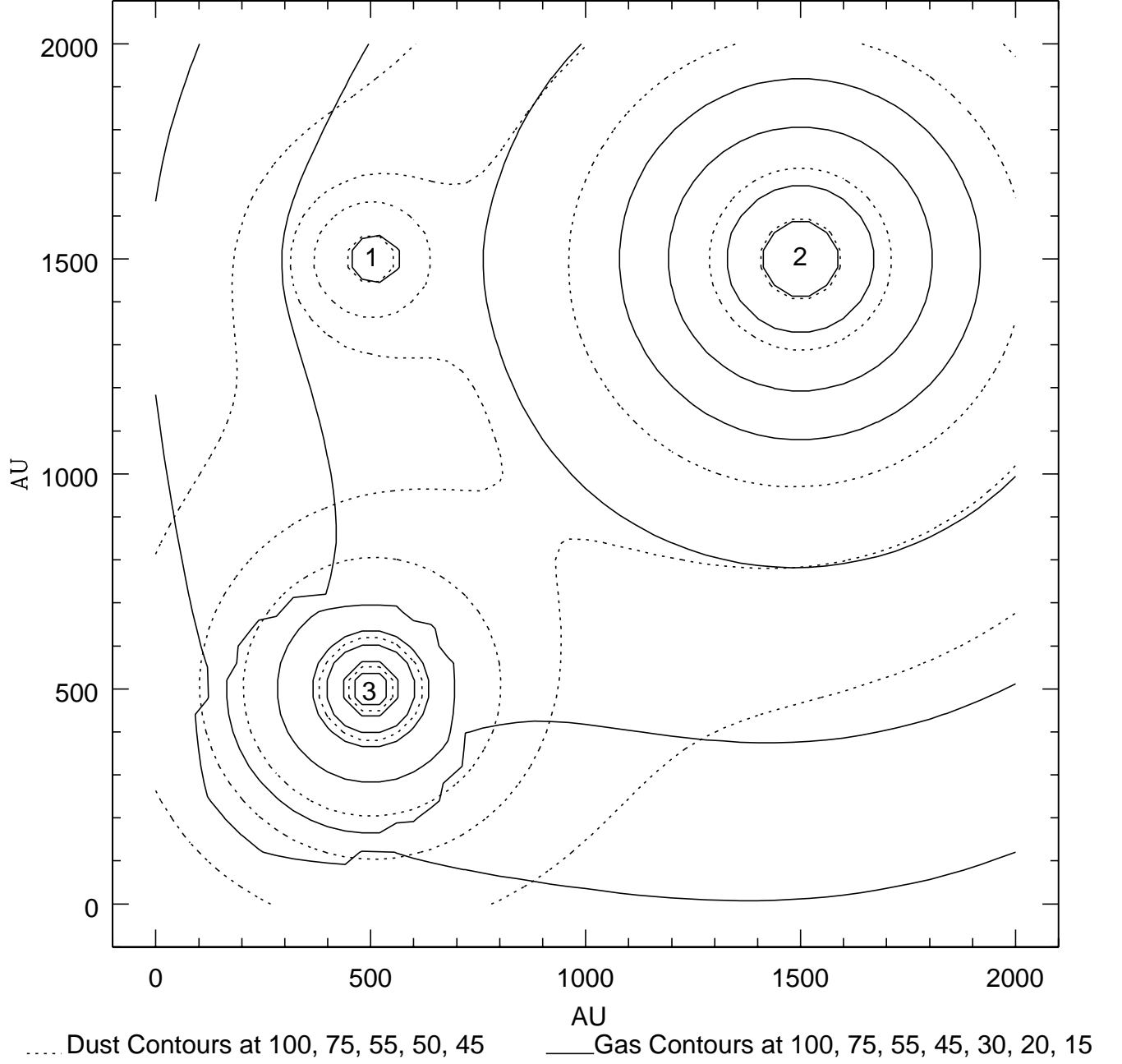


Fig. 13.— Contour plots of dust and gas temperature using the Length of Square Method. Sources are labeled according to the parameters listed in Table 4.

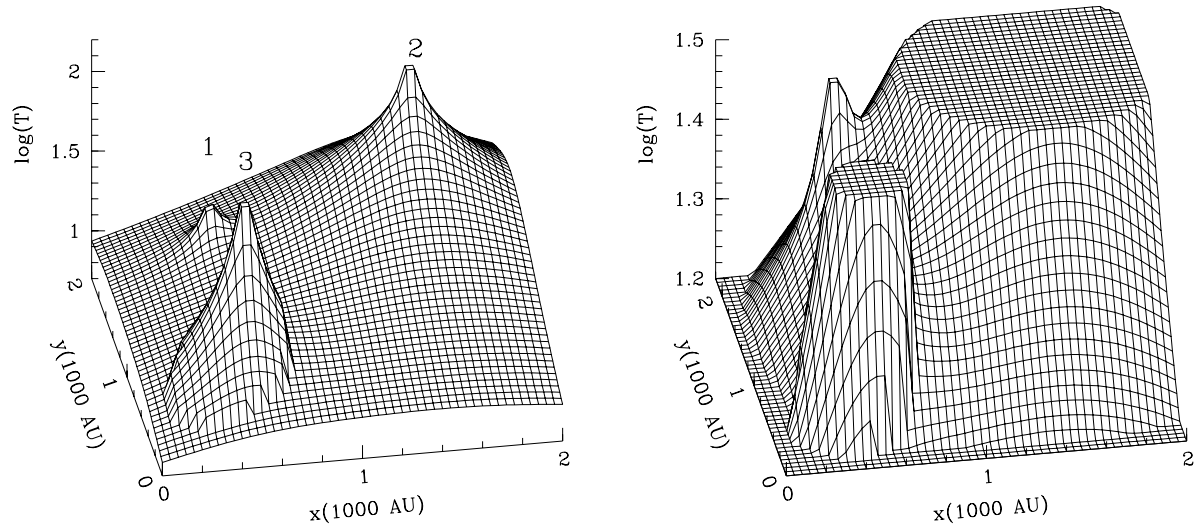


Fig. 14.— Surface plots of gas temperature using the Length of Square Method. The same data is shown in both plots with a smaller range of gas temperature shown in the second plot.

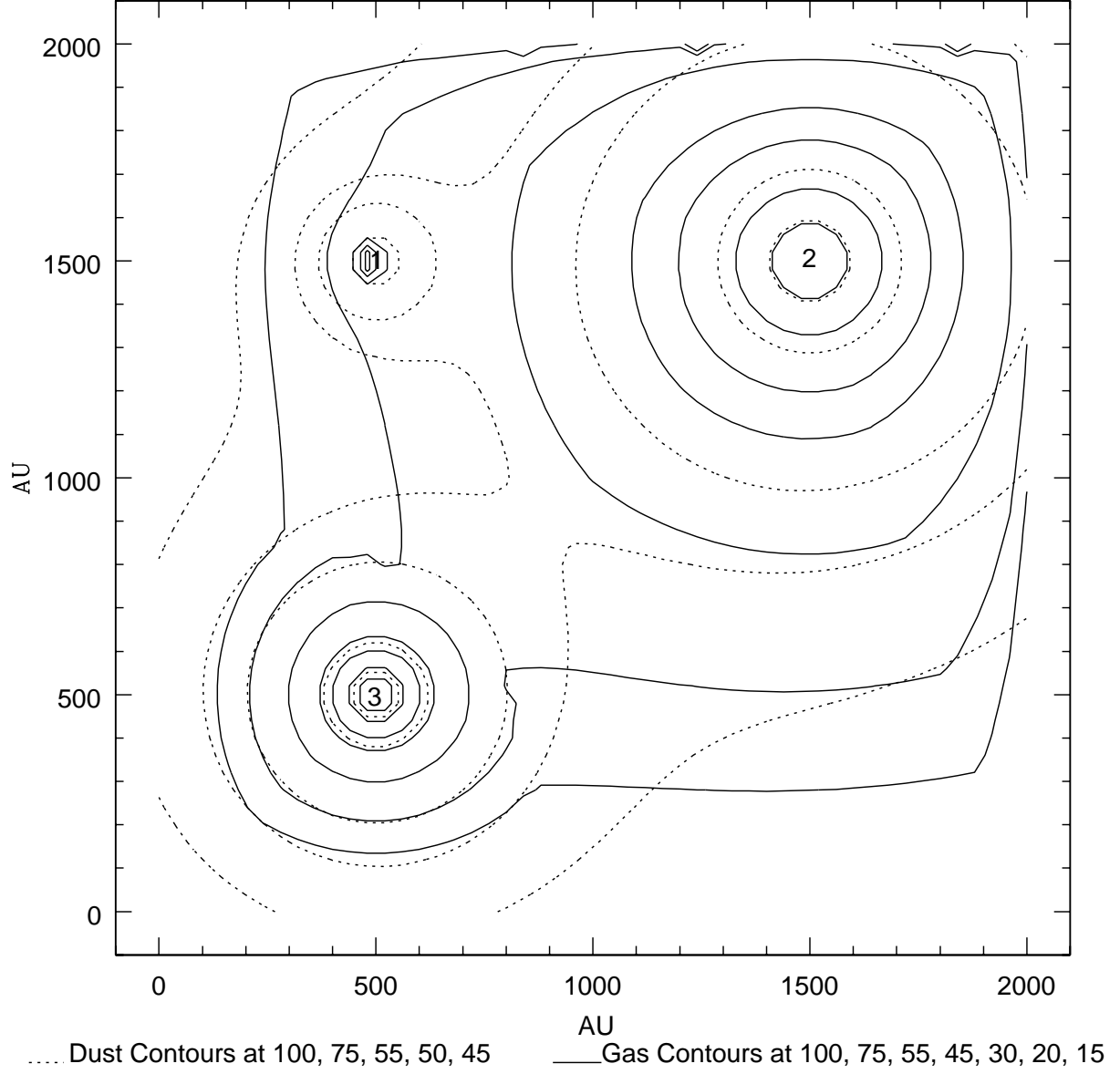


Fig. 15.— Contour plots of dust and gas temperature using the Edge of Square Method. Sources are labeled according to the parameters listed in Table 4.

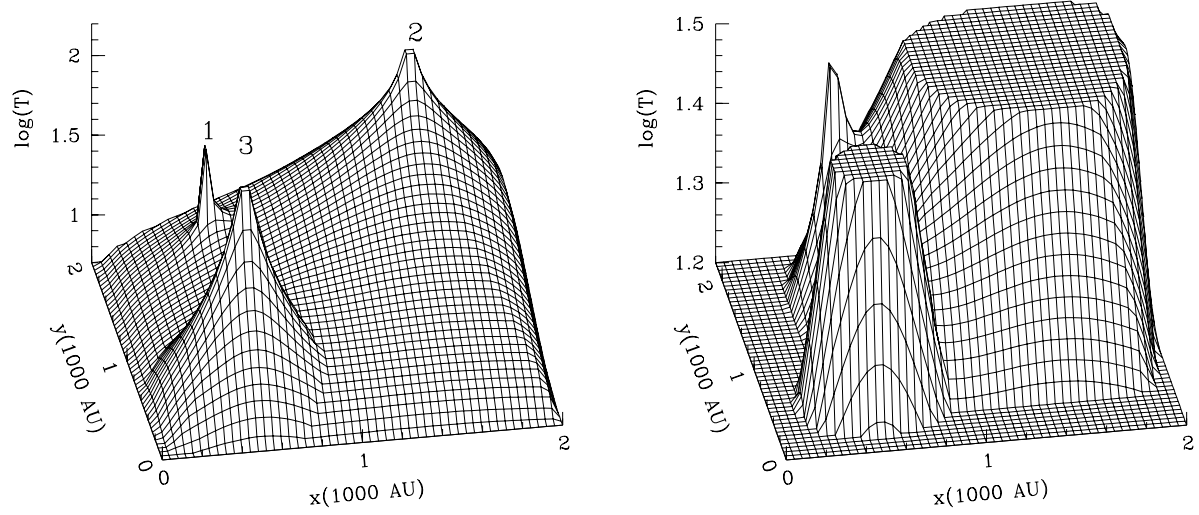


Fig. 16.— Surface plots of gas temperature using the Edge of Square Method. The same data is shown in both plots with a smaller range of gas temperature shown in the second plot.

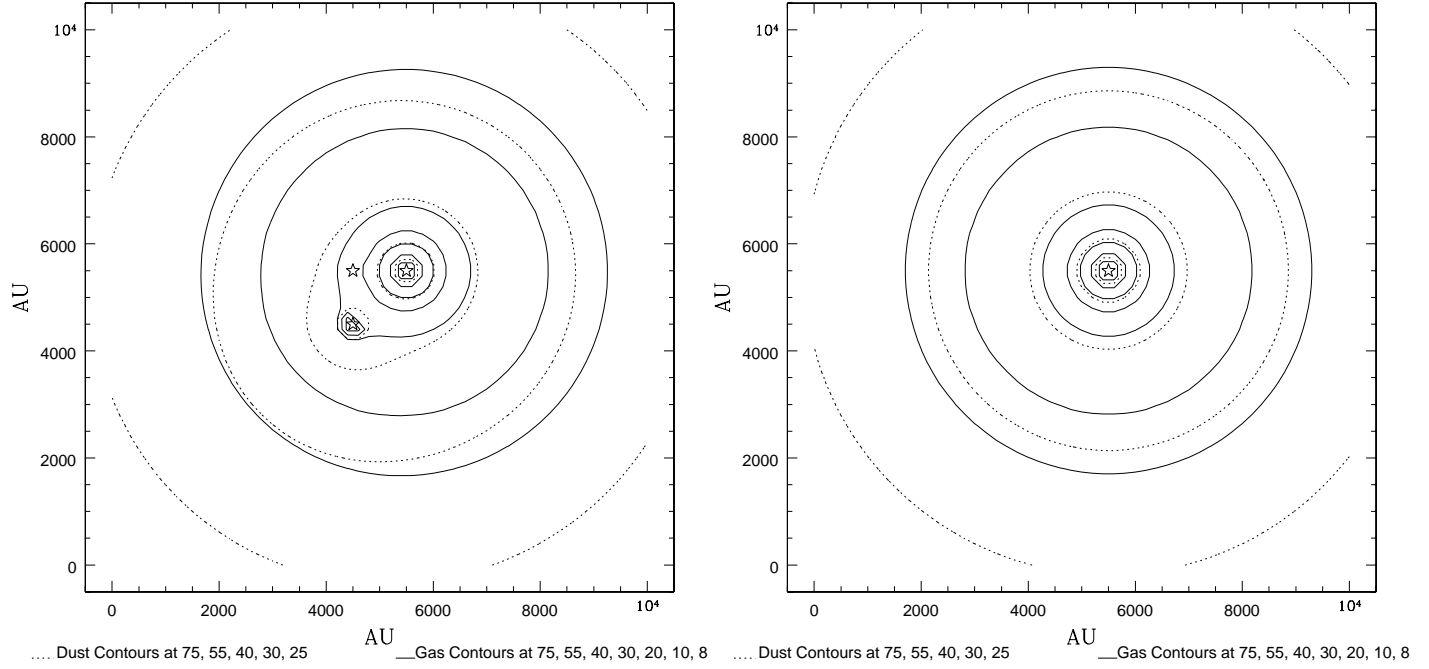


Fig. 17.— Contour plots of dust and gas temperature with three sources and one source.

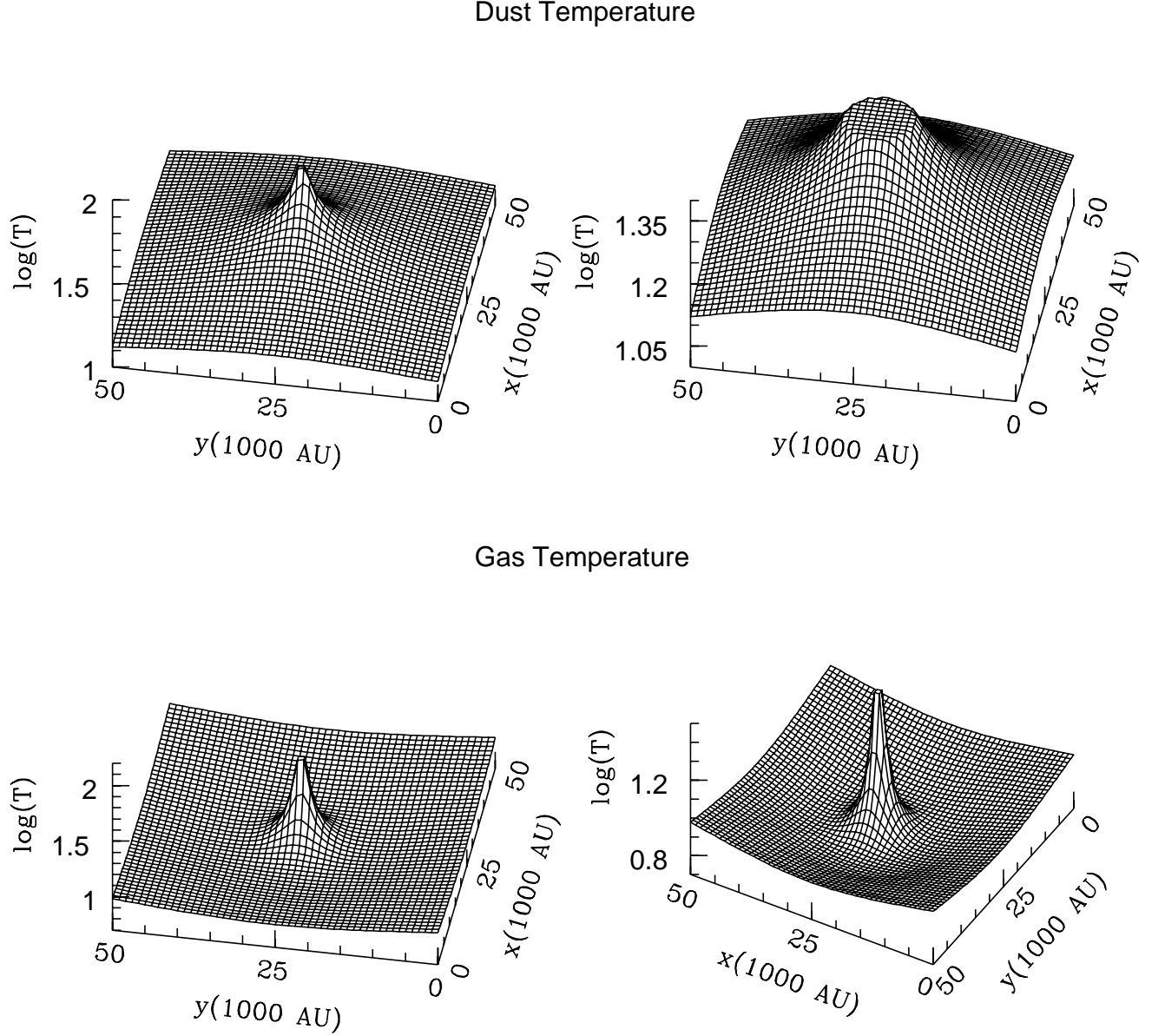


Fig. 18.— Surface plots of dust and gas temperature. Top plots show dust temperature. Bottom plots show gas temperature. Plot on top left show complete sample of dust temperatures. Top right plot shows a smaller range in dust temperatures. Bottom right and bottom left show same data from two different orientations. Area sampled is 50000 x 50000 AU. The Length of Square Method is used here.

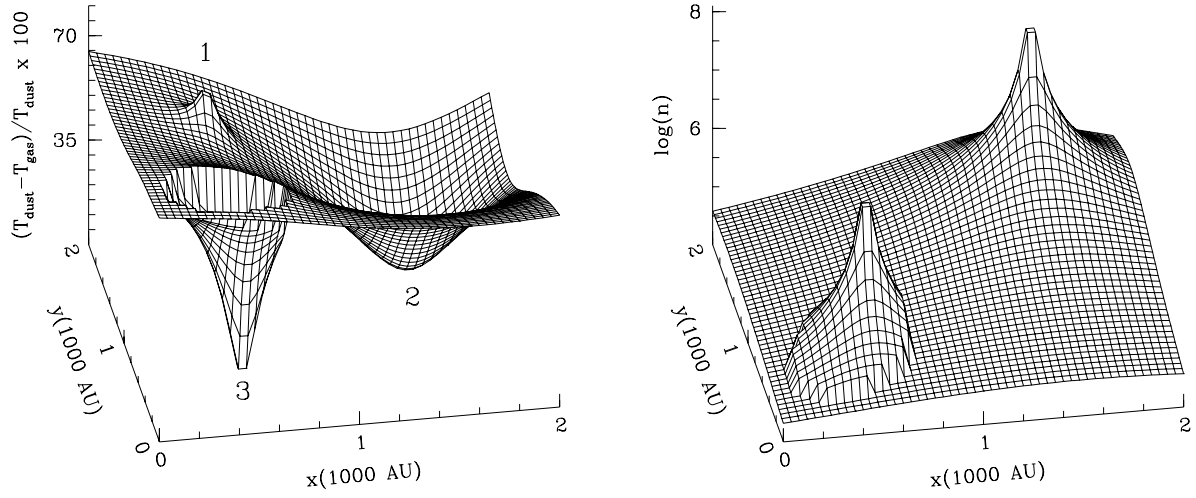


Fig. 19.— Percentage difference between gas and dust temperature and density. The same data and method as seen in Figures 12 - 14. First figure shows percentage difference of dust and gas. Second figure shows density.